Electrochimica Acta 421 (2022) 140475

Contents lists available at ScienceDirect

Electrochimica Acta

journal homepage: www.journals.elsevier.com/electrochimica-acta

Ammonia production from nitrogen under simulated solar irradiation, low overpotential, and mild conditions

Juliana Ferreira de Brito [a], Magno Barcelos Costa [a], Krishnan Rajeshwar [b], Lucia Helena Mascaro [a,*]

[a] Department of Chemistry, Federal University of São Carlos, Rod. Washington Luiz, Km 235, CEP 13565-905, São Carlos-SP, Brazil
[b] Department of Chemistry and Biochemistry, The University of Texas at Arlington, Arlington, Texas 76019-0065 USA

ARTICLE INFO

Keywords:
N_2 reduction reaction
Ammonium synthesis
Photoelectrocatalysis
Semiconductor surface modification
Fuel production

ABSTRACT

Here, we describe a strategy for the mild synthesis of ammonia (NH_3) from the photoelectrocatalytic reduction of dinitrogen. A gas diffusion layer (GDL)-confined antimony selenide photocathode decorated with platinum particles (GDL/Sb_2Se_3-Pt) was used for this purpose. The photoelectrocatalytic reduction of N_2 using GDL/Sb_2Se_3-Pt, under -0.3 $V_{Ag/AgCl}$ applied bias potential and solar irradiation (with a solar simulator and an incident intensity of 100 mW cm^{-2}), was able to produce six times more NH_3 than using the catalyst without Pt modification, reaching a value of 0.50 μmol h^{-1} cm^{-2} in a single-cell reactor with 60% Faradaic efficiency. Identical experimental conditions were applied for the photocatalysis and electrocatalysis modes, and the photoelectrocatalysis mode proved to be at least 500% more effective than the other two for NH_3 synthesis. Platinum was replaced by Pd nanoparticles with very similar outcomes showing that the noble metal role was related to its electron scavenger ability improving the charge transfer in the interface semiconductor/electrolyte. These results are deemed significant in terms of the need for substitutes to the energy-intensive Haber-Bosch process currently used for NH_3 production.

1. Introduction

The atmosphere is composed of more than 78% of dinitrogen (N_2), in a bonding state that is chemically and biologically unavailable [1]. The fixation of atmospheric N_2 is one of the most important biogeochemical cycles on this planet.[2] Accessible nitrogen is usually found in the forms of ammonia, nitrates, and urea [2]. Among these, ammonia stands out, a product produced on a large scale (more than 150 Mt per year) mainly through the Haber-Bosch process developed in the early 1920s [3]. This process takes place through the catalytic reaction between N_2 and H_2 in the presence of catalysts usually based on iron (in addition to small percentages of aluminum oxide and potassium) under high pressure (~ 200 atm) and temperature (~ 500°C) (reaction 1) [4]:

$$N_2 + 3H_2 \rightleftharpoons 2NH_3 \quad (1)$$

Despite being the main ammonia production method of the last 100 years, the energy consumption of the Haber-Bosch process is very high, representing about 1 to 3% of all the energy spent on our planet [1,5–7], in addition to consuming around 5% of the global natural gas production and generating hundreds of millions of tons of CO_2 annually [8]. These characteristics contrast with current "green" models and the search for technologies with lower CO_2 footprint and energy expenditure. In the 21st century, one of the greatest challenges for science is to develop safe, economical, and sustainable forms of energy [9]. For this reason, the production of ammonia through N_2 reduction reaction (N2RR) has been intensely studied using approaches such as enzymatic catalysis [10], electrocatalysis [3,5–7], photocatalysis [2,8,11–13], or photoelectrocatalysis [14].

Photoelectrocatalysis combining photocatalysis and electrocatalysis is an approach with many favorable attributes [15]. This technique minimizes carrier recombination in the semiconductor photocatalyst by application of a bias potential across the semiconductor/electrolyte interface [16]. The introduction of photons and the bias potential gradient (relative to the electrocatalytic and photocatalytic modes, respectively) affords an increase in the lifetime of the photogenerated charges and an improvement in charge separation, both crucial to process efficiency. Thus, photoelectrocatalysis was applied to the generation of H_2, [15,17] reduction of CO_2, [18–22] and remediation of

* Corresponding author at: Department of Chemistry, Federal University of São Carlos, Rod. Washington Luiz, Km 235, CEP 13565-905, São Carlos-SP, Brazil.
E-mail address: lmascaro@pq.cnpq.br (L.H. Mascaro).

https://doi.org/10.1016/j.electacta.2022.140475
Received 18 February 2022; Received in revised form 16 March 2022; Accepted 29 April 2022
Available online 1 May 2022

environmental pollutants such as bromides [23] and nitrates [24,25].

The number of manuscripts targeting N_2 reduction reaction by photoelectrocatalysis under room pressure and temperature is still very low. For example, a MoS_2@TiO_2 photocatalyst was used [14] under a potential of −0.2 V_{RHE} and 100 mW cm^{-2} light intensity, generating 1.42 μmol h^{-1} cm^{-2} of NH_3. $MoSe_2$@g-C_3N_4 micro/nanostructures were applied for the photochemical reduction of N_2 generating 7.72 μmol h^{-1} cm^{-2} NH_3 under −0.3 V_{RHE} and 100 mW cm^{-2} light intensity [26]. $BiVO_4$ catalyst was also investigated under ambient conditions forming 11.6 × 10^{-2} μmol h^{-1} cm^{-2} under −0.1 V_{RHE} and 100 mW cm^{-2} [27].

The innovative aspect of this study was the use of a *p*-type semiconductor (Sb_2Se_3) supported on a carbon gas diffusion layer (GDL) electrode configuration to drive the photoelectrocatalytic reduction of N_2 to NH_3. The GDL consisted of a bilayer structure formed by carbon fiber paper (a macroporous backing material) and carbon-based layer (microporous). Its morphology governed the mechanical, thermal, and electric properties, while the microporous carbon layer controlled the dispersion and stability of the electrodeposited material and the efficacy of its electron/proton transport [53]. The catalytic activity of Sb_2Se_3 was improved by Pt surface modification, a strategy that also served to improve the PEC stability of the selenide semiconductor. This composite catalyst was developed in companion work [28–33] and featured an optimal energy band gap for solar absorption (between 1.0 - 1.6 eV), a single crystal phase, and a high optical absorption coefficient (> 105 cm^{-1}) [34–36].

2. Materials and methods

2.1. Synthesis of Sb_2Se_3 modified with Pt (GDL/Sb_2Se_3-Pt)

Antimony triselenide (Sb_2Se_3) was electrodeposited on a gas diffusion layer electrode (GDL) surface using the methodology adapted from companion work [29,30,33]. To this end, an electrochemical cell fitted with three electrodes was used in conjunction with 0.5 mol L^{-1} Na_2SO_4 supporting electrolyte adjusted to pH 2 with 0.01 mol L^{-1} H_2SO_4 solution and containing the precursors 2.0 mmol L^{-1} SeO_2 and 2.5 mmol L^{-1} $K(SbO)C_4H_4O_6$. A platinum plate and an Ag/$AgCl_{(KCl\ 3M)}$ electrode were used as the counter electrode and the reference electrode respectively. Electrodeposition was carried out at a constant potential of −0.5 V and the synthesis charge was varied thus: 0.60, 1.2, 2.4, 4.8, and 9.6 C cm^{-2}. After electrodeposition, the electrodes as-prepared were calcined in a selenium atmosphere at 300 °C for 3 h with a heating ramp of 10 °C min^{-1}.

The GLD-Sb_2Se_3 catalysts were decorated with Pt nanoparticles by photoelectrodeposition. For this, a solution containing 1.0 mmol L^{-1} H_2PtCl_6 in 0.1 mol L^{-1} phosphate/0.5 mol L^{-1} Na_2SO_4 buffer at pH 6.5 was used, previously deaerated with N_2 for 15 min. The deposition was performed at a potential of −0.1 V [37] under constant solar irradiation (solar simulator, Oriel, LSC-100, with Xe lamp at 100 mW cm^{-2} and AM 1.5G filter) in a PEC cell with three electrodes and a quartz window. A Pt plate was used as a counter electrode and Ag/$AgCl/_{(KCl\ 3M)}$ as a reference electrode respectively. A charge of 60 mC cm^{-2} was employed for the deposition of Pt on the GDL/Sb_2Se_3 electrode based on companion work [33].

2.2. GDL/Sb_2Se_3 and GDL/Sb_2Se_3-Pt characterization

Morphological characterization of GDL/Sb_2Se_3 and GDL/Sb_2Se_3-Pt was performed at room temperature by X-ray powder diffraction (XRD) analysis, performed with CuKα radiation (40 kV, 30 mA) using a Shimadzu, Model XRD 6000 diffractometer with 0.5, 0.5, and 0.3 mm slits for the entrance, scattering, and exit respectively. Laser Raman spectra were obtained using a Micro Raman Horiba iHR 550 spectrophotometer and a 514 nm laser. Scanning electron microscopy (SEM) images were obtained using a FEI microscope, Model Inspect F50. X-ray photoelectron spectroscopy (XPS) was performed on a Thermo Scientific K-Alpha spectrometer using monochromatic Al Kα (1486.6 eV) radiation. Transmission electron microscopy was performed on a TECNAI G2F20 microscope-fitted EDS Zeiss equipment (Model 35); the dispersed samples were deposited on carbon-coated copper grids for this purpose.

Flat-band potential (E_{fb}) values were obtained from both Mott-Schottky (M-S) plot and linear sweep voltammetry under chopped illumination in 0.1 mol L^{-1} Na_2SO_3 supporting electrolyte. For the M-S analyses, the following equation was used [38]: $\frac{1}{C_{sc}^2} = -\frac{2}{(\varepsilon_0 \varepsilon_{sc} A^2 e N_A)}\left(E_{appl} - E_{fb} - \frac{k_B T}{e}\right)$; where C_{sc} is the capacitance of the semiconductor space charge region, ε_0 the permittivity in a vacuum, ε_{sc} the dielectric constant of the semiconductor (15 for Sb_2Se_3 [39]), A the area, e the elemental charge, N_A the density of acceptors (for *p*-type semiconductor), E_{appl} the applied potential, E_{fb} the flat-band potential, k_B the Boltzmann constant, and T the absolute temperature. The conversion of potential [vs standard hydrogen electrode (SHE)] to absolute energy [vs vacuum] was performed using the following equation [40]: Energy (vs vacuum) = − eE_{appl} (vs SHE) − 4.44 eV. In a potential range of 0.2 to 0.7 V_{RHE}, a total of 15 impedance data points were collected with 20 s of stabilization time between each point.

The conversion of the potential of Ag/AgCl/$Cl^-_{(sat.\ KCl)}$ to the reversible hydrogen electrode (RHE) scale was done using the equation [41]: E (vs RHE) = E_{appl} (vs Ag/AgCl/$Cl^-_{(sat.\ KCl)}$) + pH × 0.059 V + 0.197 V. For the linear sweep voltammetry under chopped illumination, a potentiodynamic curve was obtained with 5 mV s^{-1} and 3 s for each on/off transient. The potential range was the same in the M-S curve, and therefore, the E_{fb} is observed in the change of photocurrent behaviour. In aqueous solvent, the electrochemical N_2 reduction process involves six protons and six electrons, and can be described by the reaction [7]:

$$N_2 + 6H^+ + 6e^- \rightleftharpoons 2NH_3, E^\circ(V_{SHE}) = 0.092 - 0.059 \times pH \quad (2)$$

2.3. N_2 reduction reaction

The N2RR was performed in a completely sealed single chamber electrochemical cell with a cooling system, quartz window, and three electrodes with Ag/$AgCl_{(KCl\ 3M)}$ as the reference electrode and a Pt wire as the counter electrode. The reaction was carried out in 50 mL of 0.1 mol L^{-1} Na_2SO_3[8] in which N_2 gas was bubbled for 1 h for complete saturation of the medium, as well as throughout the entire experiment. A 30 mL acid trap of 0.005 mol L^{-1} H_3PO_4 [42] was connected to the electrochemical cell for ammonia to be collected during the reaction. Photoelectrocatalysis was performed with the Xe lamp and AM 1.5 G filter (Oriel - LSC-100, 100 mW cm^{-2}) previously described and under application of bias potential. Comparative conditions for electrocatalysis and photocatalysis techniques used the best-optimized set of variables. Aliquots were collected over the reaction time and the amount of NH_3 in all of them was analyzed by the method described next.

2.4. NH_3 detection

The rate of NH_3 production from the N_2 reduction was measured by a colorimetric method of indophenol blue using the Merck Spectroquant® commercial kit. For the 5.0 mL aliquots, sample preparation was performed by mixing 0.6 mL of the NH4-1 reagent and a micro spoon of the NH4-2 reagent (as supplied in the kit), followed by stirring and resting the solution for 5 min for complete reaction of the reagents. Then, 4 drops of the NH4-3 reagent were added from the kit own drop container, also with stirring the solution and standing for 5 min. The prepared samples were then analyzed on a UV-Vis Spectrometer (Varian, Cary 5G UV-vis-NIR) at an analytical wavelength of 690 nm. A calibration curve for NH_3 was constructed using the procedure described above in triplicate on a standard solution prepared in 0.1 mol L^{-1} Na_2SO_3 medium with concentrations ranging from 0.02 to 2.00 mg L^{-1}, as demonstrated in Fig. S1.

3. Results and Discussion

3.1. Optimization of Sb_2Se_3 electrodeposition on GDL substrate

The electrodeposition of Sb_2Se_3 on the GDL electrode surface was performed under a fixed potential. The value of the applied potential was chosen using cyclic voltammetry of the GDL electrode in 0.5 mol L^{-1} Na_2SO_4 pH 2 supporting electrolyte with and without the addition of the precursors (2.0 mmol L^{-1} SeO_2 and 2.5 mmol L^{-1} $K(SbO)C_4H_4O_6$) in solution [30]. Fig. S2 shows the data presenting a change in the current around −0.45 $V_{Ag/AgCl}$ in the presence of the precursors, indicating the moment when deposition of Sb_2Se_3 begins. According to companion work [29], in this potential regime, deposition of Se and Sb occurs simultaneously according to Eqs. 3 to 5. For this reason, a potential of −0.5 $V_{Ag/AgCl}$ was chosen for the deposition of Sb_2Se_3 on the GDL electrode surface.

$$H_2SeO_3 + 4H^+ + 4e^- \rightarrow Se + 3H_2O \quad (3)$$

$$SbO^+ + 2H^+ + 3e^- \rightarrow Sb + H_2O \quad (4)$$

$$3Se + 2Sb \rightarrow Sb_2Se_3 \quad (5)$$

From companion work [29,30], the Sb_2Se_3 electrodeposited layer must be annealed under Se atmosphere to obtain a crystalline semiconductor. XRD data of GDL/Sb_2Se_3 synthesized with 600 mC of charge previously and after thermal treatment at 300 °C and Se atmosphere is presented in Fig. S3. From the comparison of Figs. S3a and S3b, it is possible to identify in the annealed material the main peaks related to Sb_2Se_3 with spatial group *Pnma* (62) at 2θ = 28.1; 31.1; 32.1 and 34.0 with the respective peak intensities 65, 100, 64, and 52 (Fig. S3b). The other peaks present in the diffractogram are related to the GDL substrate.

As expected, thermal pre-anneal also improved the photocurrent response of the catalysts, as shown in Fig. 1a. The constant applied potential minimized the possibility of instantaneous recombination of the photogenerated charges in the Sb_2Se_3 semiconductor. Fig. 1b illustrates the influence of Sb_2Se_3 loading of the GDL substrate on the photocurrent response quality. The GDL/Sb_2Se_3 catalyst synthesized with 2.4 C cm^{-2} (blue curve) showed the highest photocurrent value among the samples evaluated, up to five times greater than that obtained for the GDL/Sb_2Se_3 electrode prepared with 1.2 C cm^{-2}. The photocurrents obtained for the semiconductors prepared with 0.60 and 1.2 C cm^{-2} (black and red curves, respectively) presented similar values, of the order of 75 μA cm^{-2}. Higher loading of Sb_2Se_3 semiconductor may be expected to generate a higher number of electrons and holes when the material is photoactivated culminating in a higher photocurrent density. Therefore, larger loadings of the GDL substrates with Sb_2Se_3 were also evaluated in relation to photoactivity (materials prepared with 4.80 and 9.60 C cm^{-2}). However, samples containing higher loadings of Sb_2Se_3 showed even lower photocurrent densities (pink and green curves, respectively) compared to catalysts prepared with a loading of 0.60 and 1.20 C cm^{-2}. While reaching the highest photocurrent response, the photocurrent obtained for the GDL/Sb_2Se_3 electrode prepared with 2.40 C cm^{-2} was not constant over time, indicating photocorrosion of the material. Further chemical modification of the optimized Sb_2Se_3/GDL surface with Pt particles was performed to address this issue.

Fig. 2a shows XPS data on GDL/Sb_2Se_3 prepared with a charge of 2.4 C cm^{-2}, presenting the peaks of Sb 3d and Se $3d_{3/2}$ in Fig. 2b and 2c, respectively. Fig. 2b shows double peaks in the region of approximately 540 and 530 eV, corresponding to Sb $3d_{3/2}$ and Sb $3d_{5/2}$, respectively, with the doublets assigned to the species, Sb_2O_3 and Sb_2Se_3 [43,44]. According to companion work [31], Sb_2O_3 oxide is naturally formed on the surfaces of Sb_2Se_3 films; however, this effect is intensified as the films undergo photocorrosion [32]. Fig. 2c shows the characteristic peak of Se $3d_{3/2}$ in the region of ~55 eV [43]. The samples were also submitted to laser Raman spectroscopy, indicating the main vibrational modes of the Sb_2Se_3 film (Fig. 2d). The peaks in the region of 80, 120, and 190 cm^{-1} were related to the orthorhombic structure of Sb_2Se_3 and the peak at ~ 240 cm^{-1} was attributed to trigonal Se, the most stable phase of selenium [45,46]. A peak from amorphous carbon at ~1340 cm^{-1}, which was attributed to the substrate [47], was also seen in these data (Fig. 2d).

3.2. Deposition of Pt particles on GDL/Sb_2Se_3

In companion work [33], we observed a remarkable improvement in the Sb_2Se_3 film stability and photocurrent response after modification of the surface with well-dispersed Pt spheres. Therefore, Pt particles were photoelectrodeposited on the GDL/Sb_2Se_3 surface using a Xe lamp with 100 mW cm^{-2} output and AM 1.5G filter and, 60 mC cm^{-2} of charge. A FE-SEM image comparing the top views of both surfaces top views is presented in Fig. 3. A similar distribution of the Sb_2Se_3 on the GDL surface was seen for both samples (Figs. 3a and 3c), and a similar shape of highly uniform cauliflower-like Sb_2Se_3 semiconductor in both cases (Figs. 3b and 3d). Additionally, the deposited Pt particles are highlighted in red (Fig. 3d), showing a circular shape and good dispersion on the Sb_2Se_3 film, with sizes ranging from 50 to 230 nm. A FE-SEM image of GDL/Sb_2Se_3-Pt with higher magnification and EDS images from two different regions showing the difference in the platinum amount in the rough spheres and in the back portion of the catalyst is presented in Fig. S4. The EDS data showed that the atomic percentage of Pt in the rough spheres was 3 times higher than in the surface with cauliflower

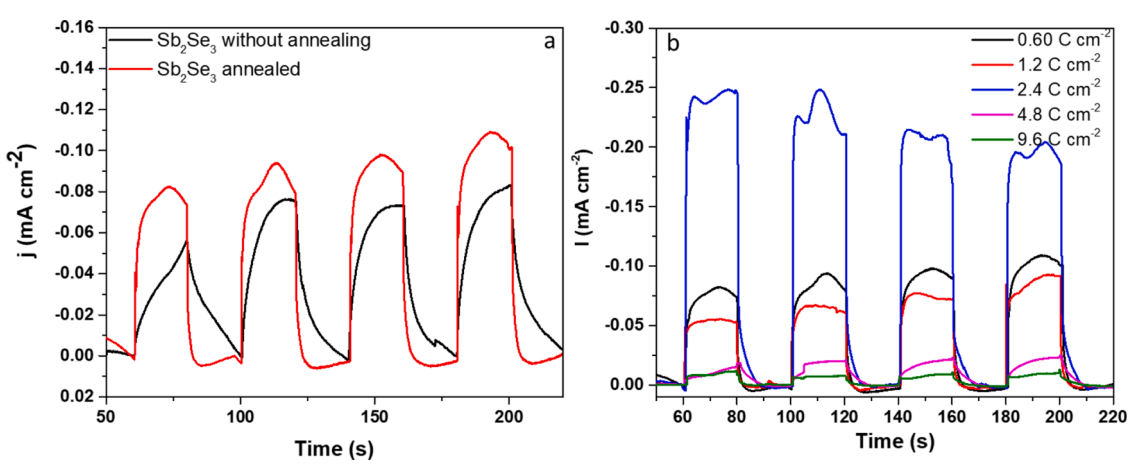

Fig. 1. Chronoamperometry scans of GDL/Sb_2Se_3 electrodes at −0.5 V in 0.1 mol L^{-1} Na_2SO_4 under transient incidence of simulated sunlight for the sample a) with and without thermal pre-anneal and b) synthesized with different values of charge.

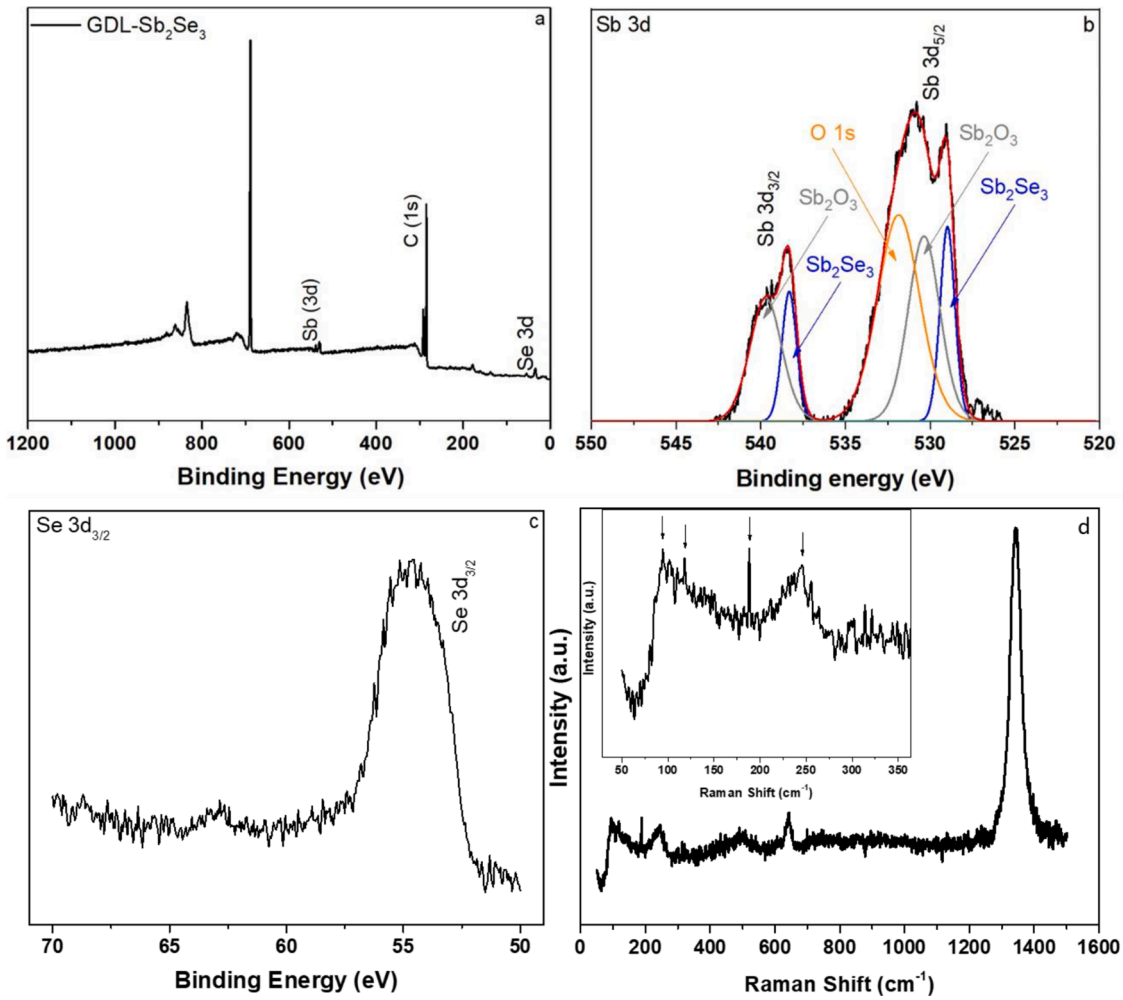

Fig. 2. XPS data for a) GDL/Sb_2Se_3, b) Sb 3d and c) Se $3d_{3/2}$. d) Laser Raman spectrum of GDL/Sb_2Se_3 with inset indicating the main vibrational modes of the semiconductor.

morphology (6.63% against 2.26%).

Identification of Pt particles deposited on the GDL/Sb_2Se_3 surface was done by XRD and laser Raman spectroscopy (Fig. S5). Through the XRD analysis (Fig. S5a) the peak with the highest intensity at $2\theta = 40.0$ could be assigned to Pt. Analyzing the Raman spectrum (Fig. S5b), it was possible to identify the presence of Pt with signals at 171 cm^{-1} and 204 cm^{-1}. The 171 cm^{-1} peak corresponds to the anti-symmetric stretching vibration mode of Pt atoms, while the 204 cm^{-1} peak corresponds to the symmetric stretching vibration mode [48]. It was also possible to observe the signals related to Sb_2Se_3 (120 cm^{-1} and 190 cm^{-1}) and a band related to Sb_2O_3 at 251 cm^{-1}. According to previous work,[48] the observation of bands in the 250 cm^{-1} region in the Raman spectrum of Sb_2Se_3 is related to incipient oxidation of this material to Sb_2O_3.

TEM images with EDS analysis (Fig. 4) were performed in order to confirm the composition of the clusters observed in the Sb_2Se_3 surface (Fig. 3). The two highlighted regions in the TEM image show the difference in composition of each morphology by EDS analysis. The EDS results demonstrated that Region 1 presented a high concentration of Pt while in Region 2, Pt was absent; instead, Sb and Se were identified, indicating that the cluster observed in the Sb_2Se_3 surface was in fact composed of Pt, corroborating the results observed in Fig. S4.

XPS provided further evidence for the presence of Pt; results of the profile fit for Pt 4f are presented in Fig. 5. Fig. 5a presents a survey XPS scan of the GDL/Sb_2Se_3-Pt sample (c.f., Fig. 2a) showing the presence of Pt in the region of 75 eV. The high-resolution Pt 4f spectrum is presented in Fig. 5b and deconvolution revealed a contribution of two Pt species according to doublets at 70.8–74.2 eV and 72.7–76.1 eV, corresponding to Pt^0 (Pt^0 $4f_{7/2}$ and Pt^0 $4f_{5/2}$) and Pt^{2+} (Pt^{2+} $4f_{5/2}$ and Pt^{2+} $4f_{7/2}$, the oxidized fraction on the surface), respectively [49].

Sb_2Se_3 semiconductor features absorption of light at wavelengths (λ) < 975 nm suggesting an indirect band gap (E_g) around 1.2 eV[33], as shown in Fig. 6a. The Tauc plot for Sb_2Se_3 and Sb_2Se_3-Pt with the extrapolation of the curves to obtain E_g showed that the presence of Pt clusters did not change the E_g value of Sb_2Se_3. Fig. 6b demonstrates the improvement in the stability of GDL/Sb_2Se_3 after surface modification with Pt particles. Chronoamperometric measurements on GDL/Sb_2Se_3-Pt under chopped sunlight (100 mW cm^{-2}) and potential of -0.5 V showed stable photocurrent flow for five complete cycles, indicating improvement in the lifetime of the electrode. This contrasts with the behavior shown earlier for GDL/Sb_2Se_3 (Fig. 1). A long-term stability test is presented in Fig. S6 under transient light incidence comparing the GDL/Sb_2Se_3 sample with and without Pt modification. After 20 min of irradiation, the GDL/Sb_2Se_3 surface starts to change in a more accentuated way than happens with the material decorated with Pt.

The FEG-SEM data showing the modification in the semiconductor surface after the long-term stability test is presented in Fig. S7. Comparing the same magnification of the images, we conclude that Pt modification is essential to the protection of the Sb_2Se_3 layer, in agreement with what was observed earlier in Fig. 1, Fig. 5, and Fig. S6. After 6750 s of transient light incidence, the morphology of the GDL/Sb_2Se_3 electrode has been completely altered to an aspect of sponges (Fig. S7a), while the morphology of the catalyst decorated with Pt was

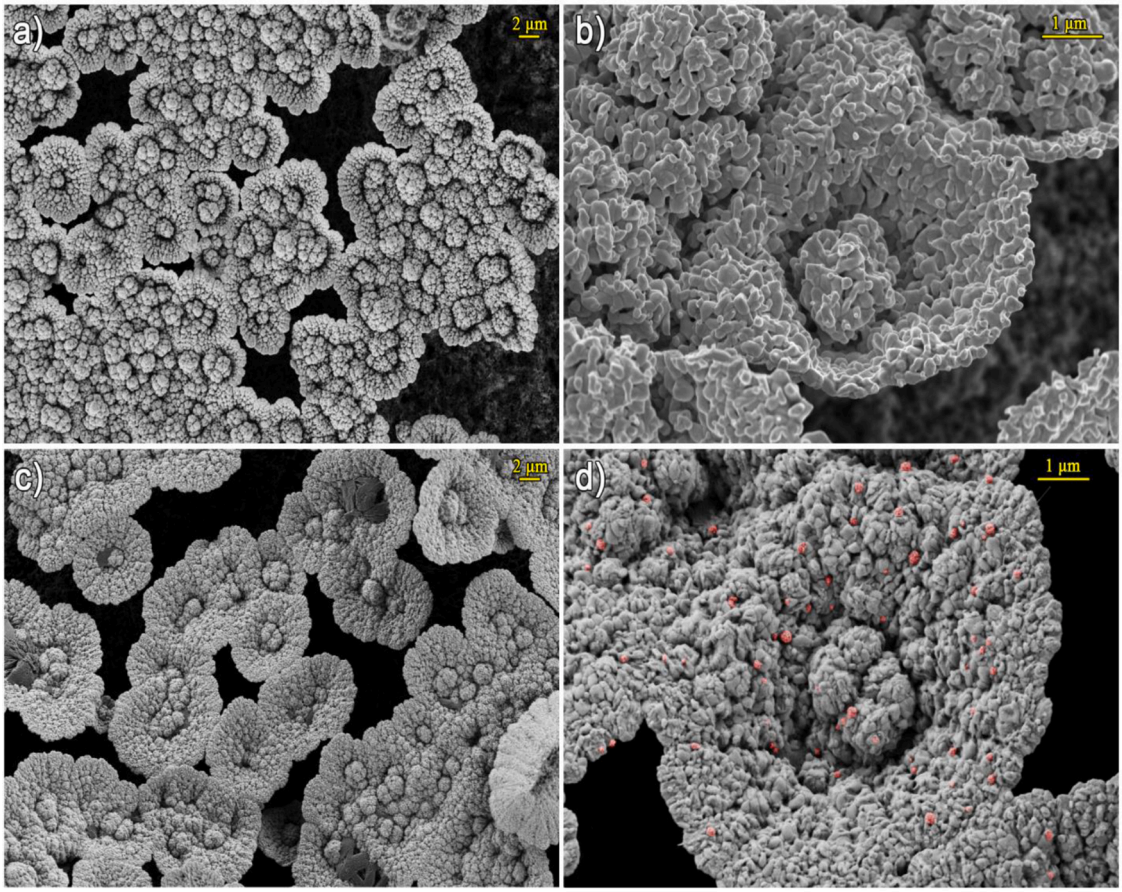

Fig. 3. FE-SEM images with different magnifications of the Sb_2Se_3/GDL electrodes without (a and b) and with (c and d) deposition of Pt particles (highlighted in red).

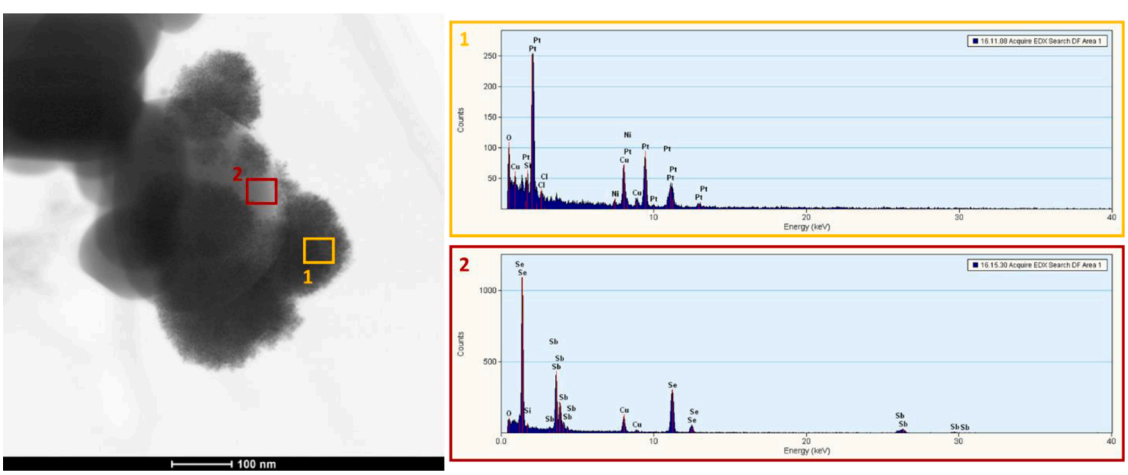

Fig. 4. TEM images of Sb_2Se_3-Pt with two different highlighted regions of EDS analysis.

maintained besides small changes in the roughness of the electrode surface (Fig. S7b).

A study of photocurrent curves during slow potentiodynamic scans under chopped illumination was employed to determine the E_{fb} of GDL/Sb_2Se_3 and GDL/Sb_2Se_3-Pt electrodes [50]. The value obtained for both catalysts was very similar, 0.57 V for GDL/Sb_2Se_3 and 0.55 V for GDL/Sb_2Se_3-Pt, just a slight change to a lower E_{fb} was obtained by the modification with Pt cluster (Fig. 7a). These values are near to the values observed in the literature for the same semiconductor [29]. The E_{fb} obtained by M-S under three different frequencies presented close values for both catalysts (Fig. S8), with the same small difference between the catalysts without modification and with Pt photoelectrodeposition, 0.46 ± 0.02 V and 0.49 ± 0.01 V. From this information, it can be assumed that the valence band (VB) for GDL/Sb_2Se_3 was −4.90 eV, while the conduction band (CB) was −3.70 eV (Fig. 7b), i.e., the VB position was identical to that observed in the literature, −4.92 eV[35].

3.3. Reduction of N_2 (N2RR) on GDL/Sb_2Se_3 and GDL/Sb_2Se_3-Pt

Linear sweep voltammetry was first performed in the dark and under irradiation with the solar simulator (100 mW cm^{-2}) in a saturated supporting electrolyte with argon (Ar) and nitrogen (N_2) gas (Fig. 8).

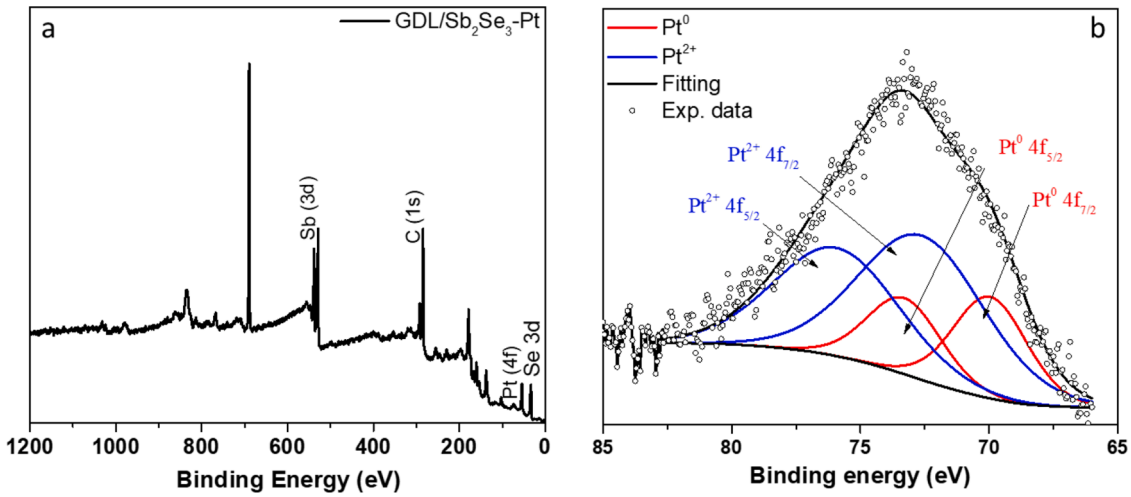

Fig. 5. XPS data in the a) survey and b) high-resolution modes in the Pt 4f binding energy regime for GDL/Sb_2Se_3-Pt.

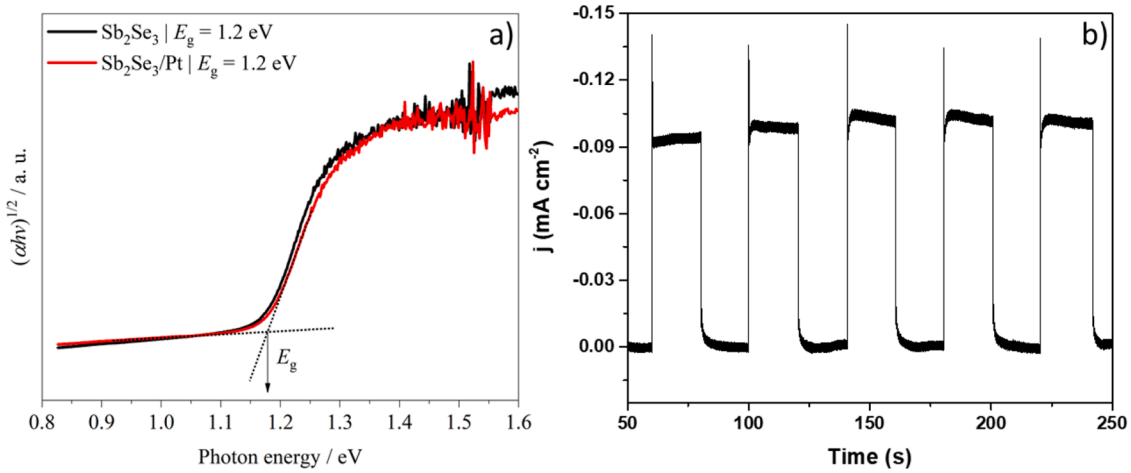

Fig. 6. a) Tauc plot for Sb_2Se_3 (black curve) and Sb_2Se_3-Pt (red curve) with extrapolation of the curves to obtain the indirect E_g and b) Chronoamperometry of GDL/Sb_2Se_3-Pt electrode at −0.5 V in 0.1 mol L^{-1} Na_2SO_4 and simulated sunlight (100 mW cm^{-2}).

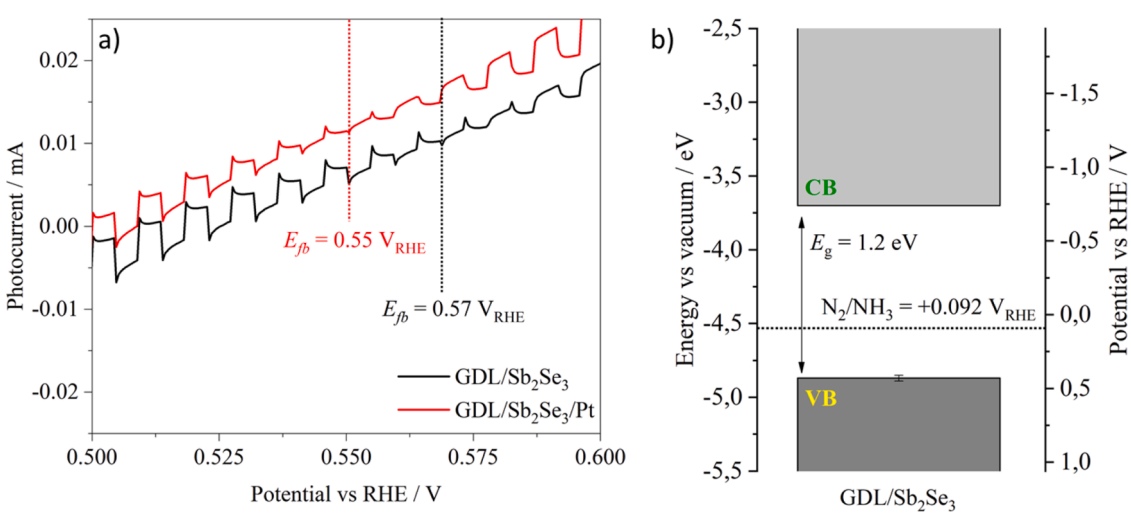

Fig. 7. a) Linear sweep voltammetry for flat band potential and b) band edge position calculated by M-S analysis.

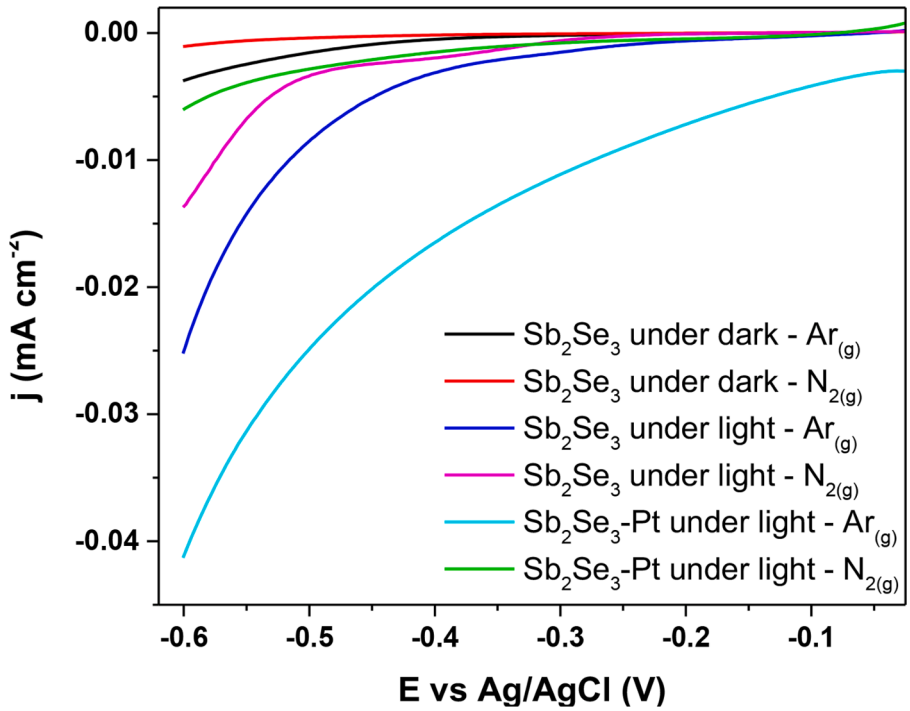

Fig. 8. Linear sweep voltammograms for GDL/Sb_2Se_3 and GDL/Sb_2Se_3-Pt in 0.1 mol L^{-1} Na_2SO_3 saturated with $Ar_{(g)}$ and $N_{2(g)}$ in the dark and under transient irradiation.

Comparing the curves with and without light incidence, an increase in cathodic current was observed under the same potential both when the semiconductor was activated by light, and when the electrolyte was saturated with Ar. The former trend is easily rationalized by the generation of electron/hole pairs (e^-/h^+) from the absorption of photons with energy equal to or greater than the band gap of the semiconductor [15,51]. On the other hand, in the comparison of the photocurrent obtained for the electrode materials with and without Pt modification in electrolytes saturated with $Ar_{(g)}$ (brown and blue curves, respectively), a large increase in current was seen at the same potential for GLD/Sb_2Se_3-Pt (compare brown and blue curves in Fig. 8). For example, at −0.4 V, the GDL/Sb_2Se_3-Pt sample presented a current of approximately −0.02 mA cm^{-2}, while GDL/Sb_2Se_3 reached a current almost an order of magnitude lower, −0.003 mA cm^{-2}.

When the supporting electrolyte was saturated with $N_{2(g)}$ instead of $Ar_{(g)}$, an inversion in the photocurrent behavior of the materials was observed. Comparing the curves obtained in the presence of $Ar_{(g)}$ and $N_{2(g)}$, for both GDL/Sb_2Se_3 (pink and blue curves, Fig. 8) and GDL/Sb_2Se_3-Pt (brown and green curves), the photocurrents obtained in $N_{2(g)}$ were lower than those obtained in $Ar_{(g)}$. This same behavior could be observed for the samples even under dark conditions (black and red curves, Fig. 7). The decrease in the current to less negative values was more pronounced for the material with Pt deposition (green curve, Fig. 8).

This behavior is diagnostic of adsorption of $N_{2(g)}$ on the composite electrode surface, possibly causing a decrease in the number of available sites for activation of the semiconductor culminating in a decrease in the current when compared to the voltammetry obtained in $Ar_{(g)}$. Similar behavior was also observed by other researchers [52]. A decrease of current density due to CO_2 adsorption on the catalyst surface was also observed for CO_2RR. [53], underlining that adsorption is an important pre-requisite for the electroreduction of chemically and electrochemically inert molecules such as N_2 or CO_2. For reduction to be facilitated, it is necessary to first adsorb the molecules on the semiconductor surface, so that subsequent protonation/electronation events (Fig. 10) can take place [54]. In the absence of $N_{2(g)}$ and presence of $Ar_{(g)}$, there is no reactant to adsorb in the electrode surface, so all the available sites are free to reduce water generating H_2 and culminating in a higher current density as observed for the GDL/Sb_2Se_3 and GDL/Sb_2Se_3-Pt electrodes.

The photoelectrocatalysis technique was used under different potentials and incidence of sunlight (solar simulator with an intensity of 100 mW cm^{-2} and AM 1.5G filter) for both GDL/Sb_2Se_3 and GDL/Sb_2Se_3-Pt. The best reaction condition was compared using photocatalysis and electrocatalysis modes. Ammonia production was detected by the indophenol blue method (Fig. S8). The results for NH_3 production are shown in Fig. 9a; the GDL/Sb_2Se_3-Pt sample showed better performance for N2RR than GDL/Sb_2Se_3, as could be anticipated from the data in Fig. 8.

A potential of −0.3 V was optimal for NH_3 synthesis using GDL/Sb_2Se_3-Pt, where a production rate of approximately 0.50 μmol h^{-1} cm^{-2} was achieved. For GDL/Sb_2Se_3, the quantity produced was at least six times lower applying the same condition.

To confirm that Pt particles on the semiconductor surface improve charge transfer by trapping the electrons from the Sb_2Se_3 conduction band and minimizing the electron/hole recombination, an electrode was constructed under the same conditions with the same amount of noble metal, however, modified with palladium (Pd) instead Pt. The FEG-SEM image showing the top view of the Sb_2Se_3 semiconductor modified with well-dispersed nanoparticles confirmed to be Pd by EDS is presented in Fig. S9. The synthesis of Pd was performed with the same proportional charge (30 mC cm^{-2}) used for Pt deposition, and according to the EDS, the atomic percentage of Pd was 7.90%, close to the 6.63% obtained for Pt. As can be observed in Fig. 9a, a difference of just 2% was obtained in the production of NH_3 modifying the semiconductor with Pd instead of Pt, proving that the contribution of the metal is related to its electron scavenger ability, which is essential in the case of Sb_2Se_3 semiconductor. The similarity of the results obtained with Pd and Pt nanoparticles is in congruence with the volcano plots and the proximity of the Gibbs free energy for both materials in relation to the potential of the limiting steps for N_2 reduction reaction [5].

Fig. 9b shows chronoamperometry data on both materials applying −0.3 V potential under the influence of light pulses with a duration of 20

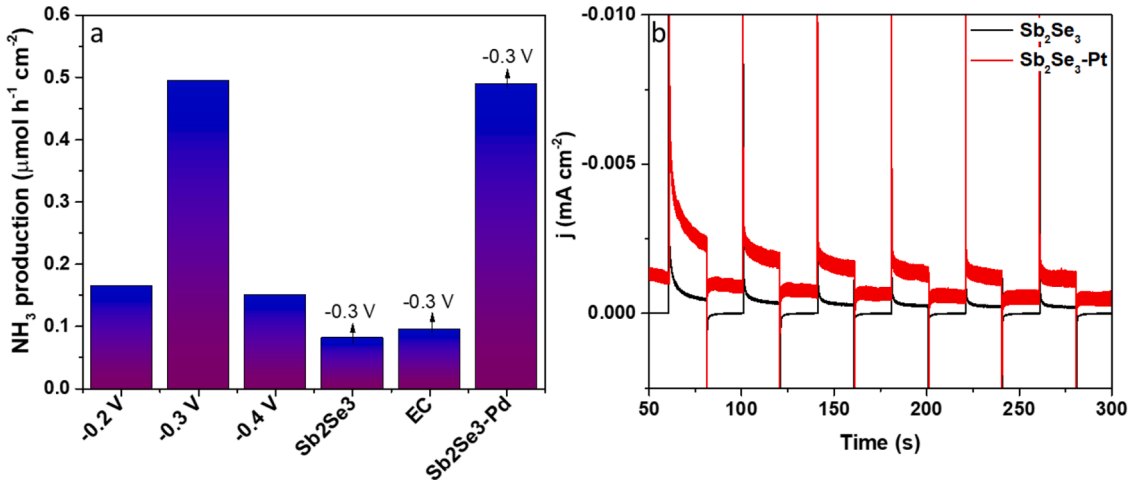

Fig. 9. a) NH_3 production using photoelectrocatalysis (under three bias potentials), and electrocatalysis and photoelectrocatalysis at −0.3 V for GDL/Sb_2Se_3-Pt, GDL/Sb_2Se_3, and GDL/Sb_2Se_3-Pd, respectively; and b) Chronoamperometry for the GDL/Sb_2Se_3-Pt (red curve) and GDL/Sb_2Se_3 (black curve) at −0.3 V and transient irradiation.

s, in supporting electrolyte saturated with $N_{2(g)}$. The electrode with Pt particles presented a higher photocurrent than the sample without co-catalyst modification. In both cases, the initial spikes decayed to a steady-state almost instantly, forming the characteristic plateau reflecting charge extraction and charge recombination in the semiconductor [55]. However, the spike for GDL/Sb_2Se_3-Pt reached more negative (cathodic) currents than for GDL/Sb_2Se_3.

Fig. 10 presents a reaction mechanism visualized for the reduction of N_2 with NH_3 generation on our GDL/Sb_2Se_3-Pt samples using the photoelectrocatalysis mode. In this mechanism, the Sb_2Se_3 semiconductor is first activated by the action of light and potential, exciting the electrons in the valence band (VB) to the conduction band (CB) and generating holes in the VB. The Pt particles photoelectrodeposited on the semiconductor surface trap the electrons present in the CB, as happens with other metals on different semiconductors, thus minimizing the recombination of the photogenerated charges [19,56,57]. A major function of Pt is also to serve as a site for protonation of the nitrogen molecule and the intermediates leading ultimately to the ammonia product.

The pH of the Na_2SO_3 supporting electrolyte changed drastically after the reaction, starting at pH 10 and decreasing to ~ 4, indicating the occurrence of water oxidation reaction with proton formation. Remembering that N2RR with the generation of 2 NH_3 molecules requires 6 electrons and 6 protons to occur [3,54], and considering the volume of the acid trap from where the aliquots were analyzed, the Faradaic efficiency for the optimized condition reached 60%. Without Pt co-catalyst, protonation could not occur accounting for the negligible N2RR activity observed here for the GDL/Sb_2Se_3 samples.

Finally, Table 1 compares the results from this study with previous data on NH_3 production from the literature. Direct comparisons are obviated by the different experimental conditions and the lack of a self-consistent set of metrics for the product generation rate attained; however, the present results compare very favorably.

4. Conclusions

The present work described the optimization and characterization of GDL/Sb_2Se_3 prepared by electrodeposition, as well as its chemical modification with Pt particles by photoelectrodeposition. Both types of

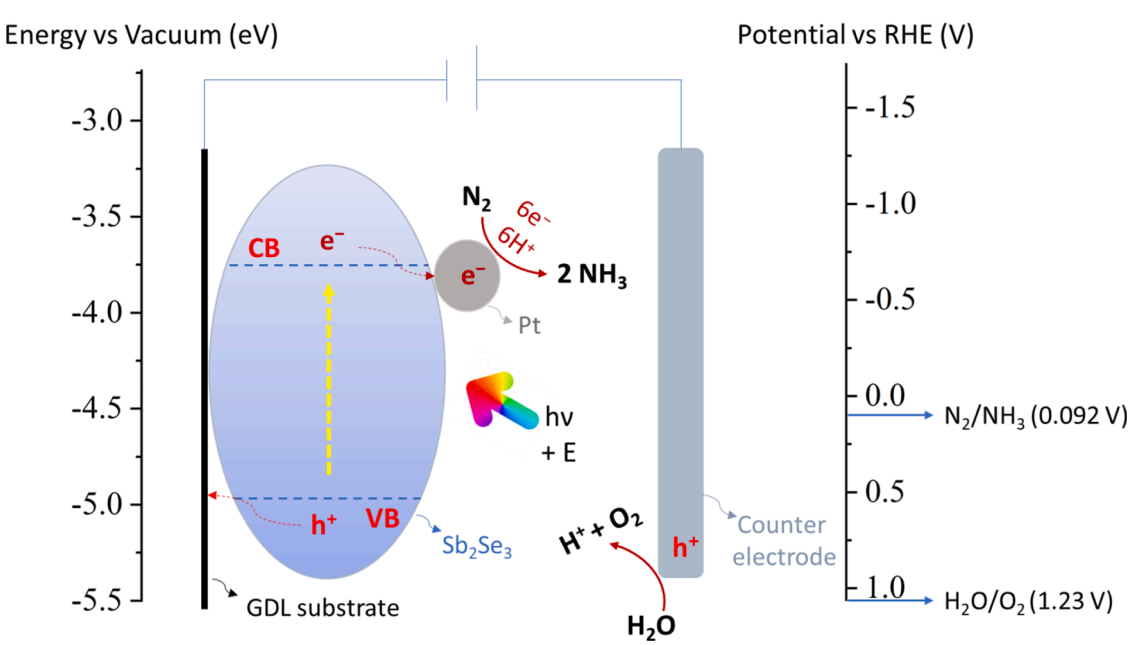

Fig. 10. Reaction mechanism visualized for the reduction of N_2 on GDL/Sb_2Se_3-Pt using the photoelectrocatalysis mode.

Table 1
Comparison of present data with N_2 reduction at room temperature and atmospheric pressure and NH_3 production metrics from the literature.

Catalyst	Experimental Conditions	NH_3 Concentration (detection method)	Ref.
ECG diamond	PC[a] in N_2-saturated water using dual-compartment cells and 450 W high-pressure Hg/Xe lamp.	1.3 μg h^{-1} (indophenol blue method)	[58]
GNP/bSi/Cr	PC in 150 ppm Na_2SO_3 N_2-saturated, 300 W Xe lamp (200 mW cm^{-2}).	13.3 mg m^{-2} h^{-1} (ammonia/ammonium ISE and indophenol blue method)	[8]
Pd-TiO_2	PC in 400 ml of deionized water with 121 ppm of KNO_3 and N_2-saturated using a one-compartment reactor, 400 W UV lamp, and 0.5 g of the photocatalyst.	7.06 μmol h^{-1} NH_3 (indophenol blue method)	[59]
AlNTs – TiO_2	PC in 10% ethanol aqueous solution N_2-saturated at pH 4, LED at 365 nm (5 mW cm^{-2}).	0.1 mmol L^{-1} h^{-1} mW^{-1} cm^{-2} (standard colorimetric assay for ammonium chloride)	[60]
MoS_2@TiO_2	PEC[b] in 0.1 M Na_2SO_4, saturated with N_2 using two-chamber H-type cell, Xe lamp (100 mW cm^{-2}), and potential of -0.3 V_{RHE}.	1.42 μmol h^{-1} cm^{-2} (indophenol blue method)	[14]
$MoSe_2$@g-C_3N_4	PEC in 0.1 M KOH, saturated with N_2 using two-chamber H-type cell, Xe lamp (100 mW cm^{-2}), and potential of -0.3 V_{RHE}.	7.72 μmol h^{-1} cm^{-2} (indophenol blue method)	[26]
$BiVO_4$	PEC in 0.1 M Li_2SO_4, saturated with N_2 using two-chamber H-type cell, Xe lamp (100 mW cm^{-2}), and potential of -0.1 V_{RHE}.	1.16 nmol h^{-1} cm^{-2} (Nessler's reagent spectrophotometry)	[27]
GDL/ Sb_2Se_3-Pt	PEC in 0.1 mol L^{-1} Na_2SO_3 using one-chamber cell, -0.3 $V_{Ag/AgCl}$ and Xe lamp (100 mW cm^{-2}).	0.50 μmol h^{-1} cm^{-2} (indophenol blue method)	This study

[a] PC = photocatalysis.
[b] PEC = photoelectrocatalysis.

samples: GDL/Sb_2Se_3 and GDL/Sb_2Se_3-Pt, were employed for N2RR using the photoelectrocatalysis technique successfully generating NH_3. However, GDL/Sb_2Se_3-Pt was the more effective catalyst for NH_3 production, attaining 0.50 μmol h^{-1} cm^{-2} under −0.3 $V_{Ag/AgCl}$ and sunlight incidence with 60% Faradaic efficiency, while NH_3 synthesis with GDL/Sb_2Se_3 reached a value at least six times lower under the same reaction conditions. The insertion of Pd nanoparticles instead of Pt nanoparticles brought about similar results, showing that the metal role was indeed related to its electron scavenger ability improving the charge transfer of the Sb_2Se_3 photocatalyst. The photoelectrocatalysis mode proved to be more effective than the photocatalysis and electrocatalysis counterpart modes for the synthesis of NH_3 with a yield at least 500% higher.

Authorship contribution statement

Juliana F. Brito: Investigation, methodology, data curation, writing - original draft, writing - review & editing. **Magno B. Costa:** Investigation, writing - original draft, writing - review & editing. **Krishnan Rajeshwar:** Visualization, writing - review & editing. **Lucia H. Mascaro:** Visualization, supervision, writing - review & editing, resources.

Funding

This work was supported by the São Paulo Research Foundation, FAPESP [Grant numbers #2018/02950-0, #2017/21365-8, #2018/26005-2, #2018/16401-8, #2013/07296-2, #2014/50249-8 and #2017/11986-5]; Conselho Nacional de Desenvolvimento Científico e Tecnológico, CNPq [Grant number 152471/2018-9]; and Coordenação de Aperfeiçoamento de Pessoal de Nível Superior - Brasil, CAPES [Grant number 001].

Declaration of Competing Interest

The authors declare that they have no known competing financial interests or personal relationships that could have appeared to influence the work reported in this paper.

Acknowledgment

The authors thank the Laboratory of Structural Characterization, LCE/DEMa/UFSCar, for general facilities.

Supplementary materials

Supplementary material associated with this article can be found, in the online version, at doi:10.1016/j.electacta.2022.140475.

References

[1] J.W. Erisman, M.A. Sutton, J. Galloway, Z. Klimont, W. Winiwarter, How a century of ammonia synthesis changed the world, Nat. Geosci. 1 (2008) 636–639, https://doi.org/10.1038/ngeo325.
[2] A.J. Medford, M.C. Hatzell, Photon-driven nitrogen fixation: current progress, thermodynamic considerations, and future outlook, ACS Catal. 7 (2017) 2624–2643, https://doi.org/10.1021/acscatal.7b00439.
[3] S. Chen, S. Perathoner, C. Ampelli, C. Mebrahtu, D. Su, G. Centi, Electrocatalytic synthesis of ammonia at room temperature and atmospheric pressure from water and nitrogen on a carbon-nanotube-based electrocatalyst, Angew, Chemie - Int. Ed. 56 (2017) 2699–2703, https://doi.org/10.1002/anie.201609533.
[4] V. Kyriakou, I. Garagounis, E. Vasileiou, A. Vourros, M. Stoukides, Progress in the electrochemical synthesis of ammonia, Catal. Today 286 (2017) 2–13, https://doi.org/10.1016/j.cattod.2016.06.014.
[5] J.H. Montoya, C. Tsai, A. Vojvodic, J.K. Nørskov, The challenge of electrochemical ammonia synthesis: A new perspective on the role of nitrogen scaling relations, ChemSusChem 8 (2015) 2180–2186, https://doi.org/10.1002/cssc.201500322.
[6] S.-J. Li, D. Bao, M.-M. Shi, B.-R. Wulan, J.-M. Yan, Q. Jiang, Amorphizing of Au nanoparticles by CeOx -RGO hybrid support towards highly efficient electrocatalyst for N2 reduction under ambient conditions, Adv. Mater 29 (2017), 1700001, https://doi.org/10.1002/adma.201700001.
[7] B.M. Lindley, A.M. Appel, K. Krogh-Jespersen, J.M. Mayer, A.J.M. Miller, Evaluating the thermodynamics of electrocatalytic N2 reduction in acetonitrile, ACS Energy Lett (2016) 698–704, https://doi.org/10.1021/acsenergylett.6b00319.
[8] M. Ali, F. Zhou, K. Chen, C. Kotzur, C. Xiao, L. Bourgeois, X. Zhang, D. R. MacFarlane, Nanostructured photoelectrochemical solar cell for nitrogen reduction using plasmon-enhanced black silicon, Nat. Commun. 7 (2016) 11335, https://doi.org/10.1038/ncomms11335.
[9] A. Grinberg Dana, O. Elishav, A. Bardow, G.E. Shter, G.S. Grader, Nitrogen-based fuels: a power-to-fuel-to-power analysis, Angew, Chemie - Int. Ed 55 (2016) 8798–8805, https://doi.org/10.1002/anie.201510618.
[10] S. Shaw, D. Lukoyanov, K. Danyal, D.R. Dean, B.M. Hoffman, L.C. Seefeldt, Nitrite and hydroxylamine as nitrogenase substrates: Mechanistic implications for the pathway of N2 reduction, J. Am. Chem. Soc 136 (2014) 12776–12783, https://doi.org/10.1021/ja507123d.
[11] J.R. Christianson, D. Zhu, R.J. Hamer, J.R. Schmidt, Mechanism of N2 reduction to NH3 by aqueous solvated electrons, J. Phys. Chem. B 118 (2014) 195–203, https://doi.org/10.1021/jp406535p.
[12] T.D. Schrauzer, N. Guth, Photolysis of water and photoreduction of nitrogen on titanium dioxide, J. Am. Chem. Soc 99 (1977) 7189–7193, https://doi.org/10.1021/ja00464a015.
[13] H. Miyama, N. Fujii, Y. Nagae, Heterogeneous photocatalytic synthesis of ammonia from water and nitrogen, Chem. Phys. Lett 74 (1980) 523–524, https://doi.org/10.1016/0009-2614(80)85266-3.
[14] W. Ye, M. Arif, X. Fang, M.A. Mushtaq, X. Chen, D. Yan, Efficient photoelectrochemical route for the ambient reduction of N2 to NH3 based on nanojunctions assembled from MoS2 nanosheets and TiO2, ACS Appl, Mater. Interfaces 11 (2019) 28809–28817, https://doi.org/10.1021/acsami.9b06596.

[15] G.G. Bessegato, T.T. Guaraldo, J.F. de Brito, M.F. Brugnera, M.V.B. Zanoni, Achievements and trends in photoelectrocatalysis: from environmental to energy applications, Electrocatalysis 6 (2015) 415–441, https://doi.org/10.1007/s12678-015-0259-9.
[16] C. Li, T. Wang, Z.-J. Zhao, W. Yang, J.-F. Li, A. Li, Z. Yang, G.A. Ozin, J. Gong, Promoted fixation of molecular nitrogen with surface oxygen vacancies on plasmon-enhanced TiO2 photoelectrodes, Angew, Chemie Int. Ed 57 (2018) 5278–5282, https://doi.org/10.1002/anie.201713229.
[17] T.T. Guaraldo, V.R. Gonçales, B.F. Silva, S.I.C. De Torresi, M.V.B. Zanoni, Hydrogen production and simultaneous photoelectrocatalytic pollutant oxidation using a TiO2/WO3 nanostructured photoanode under visible light irradiation, J. Electroanal. Chem 765 (2016) 188–196, https://doi.org/10.1016/j.jelechem.2015.07.034.
[18] J.F. Brito, A.A. Silva, A.J. Cavalheiro, M.V.B. Zanoni, Evaluation of the parameters affecting the photoelectrocatalytic reduction of CO2 to CH3OH at Cu/Cu2O electrode, Int. J. Electrochem. Sci 9 (2014) 5961–5973.
[19] T.T. Guaraldo, J.F. de Brito, D Wood, M.V.B. Zanoni, A new Si/TiO2/Pt p-n junction semiconductor to demonstrate photoelectrochemical CO2 conversion, Electrochim, Acta 185 (2015) 117–124, https://doi.org/10.1016/j.electacta.2015.10.077.
[20] S. Stülp, J.C. Cardoso, J.F. de Brito, J.B.S. Flor, R.C.G. Frem, F.A. Sayão, M.V. B. Zanoni, An artificial photosynthesis system based on Ti/TiO2 coated with Cu(II) aspirinate complex for CO2 reduction to methanol, Electrocatalysis (2017) 1–9, https://doi.org/10.1007/s12678-017-0367-9.
[21] J.F. de Brito, M.V.B. Zanoni, On the application of Ti/TiO2/CuO n-p junction semiconductor: a case study of electrolyte, temperature and potential influence on CO2 reduction, Chem, Eng. J. 318 (2017) 264–271, https://doi.org/10.1016/j.cej.2016.08.033.
[22] G. Ghadimkhani, N.R. de Tacconi, W. Chanmanee, C. Janaky, K. Rajeshwar, Efficient solar photoelectrosynthesis of methanol from carbon dioxide using hybrid CuO-Cu2O semiconductor nanorod arrays, Chem. Commun 49 (2013) 1297–1299, https://doi.org/10.1039/c2cc38068d. Camb.
[23] F.M.M. Paschoal, G. Pepping, M.V.B. Zanoni, M.A. Anderson, Photoelectrocatalytic removal of bromate using Ti/TiO2 coated as a photocathode, Environ, Sci. Technol 43 (2009) 7496–7502, https://doi.org/10.1021/es803366d.
[24] F.A. Sayão, L. Nuñez, M.V.B. Zanoni, Efficient photoelectrochemical reduction of nitrite to ammonium and nitrogen containing gaseous species using Ti/TiO2 nanotube electrodes, J. Braz, Chem. Soc 25 (2014) 1153–1160, https://doi.org/10.5935/0103-5053.20140091.
[25] F.M.M. Paschoal, L. Nuñez, M.R.D.V. Lanza, M.V.B. Zanoni, Nitrate removal on a Cu/Cu2O photocathode under UV irradiation and bias potential, J. Adv. Oxid. Technol 16 (2013) 63–70.
[26] M.A. Mushtaq, M. Arif, X. Fang, G. Yasin, W. Ye, M. Basharat, B. Zhou, S. Yang, S. Ji, D. Yan, Photoelectrochemical reduction of N2 to NH3 under ambient conditions through hierarchical MoSe2@g-C3N4 heterojunctions, J. Mater, Chem. A. 9 (2021) 2742–2753, https://doi.org/10.1039/d0ta10620h.
[27] Y. Bai, J. Lu, H. Bai, Z. Fang, F. Wang, Y. Liu, D. Sun, B. Luo, W. Fan, W. Shi, Understanding the key role of vanadium in p-type BiVO4 for photoelectrochemical N2 fixation, Chem. Eng. J. 414 (2021), 128773, https://doi.org/10.1016/j.cej.2021.128773.
[28] M.B. Costa, F.W. de, S. Lucas, L.H. Mascaro, Thermal treatment effects on electrodeposited Sb2Se3 photovoltaic thin films, ChemElectroChem 4 (2017) 2507–2514, https://doi.org/10.1002/celc.201700511.
[29] M.B. Costa, F.W. de, S. Lucas, L.H. Mascaro, Electrodeposition of Fe-doped Sb2Se3 thin films for photoelectrochemical applications and study of the doping effects on their properties, J. Solid State Electrochem. (2017) 1–6, https://doi.org/10.1007/s10008-017-3768-z.
[30] M.B. Costa, F.W.S. Lucas, L.H. Mascaro, Electrodeposition conditions effect Sb2Se3 thin-film properties, ChemElectroChem 6 (2019) 2937–2944, https://doi.org/10.1002/celc.201900457.
[31] M.B. Costa, F.W.S. Lucas, L.H. Mascaro, Improvement of electrodeposited Sb2Se3 thin film photoelectroactivity by cobalt grain boundary modification, J. Mater. Chem. A 8 (2020) 13742–13753, https://doi.org/10.1039/D0TA03160G.
[32] M.B. Costa, F.W.S. Lucas, M. Medina, L.H. Mascaro, All-electrochemically grown Sb2Se3/a-MoSx photocathodes for hydrogen production: the effect of the MoSx layer on the surface recombination and photocorrosion of Sb2Se3 films, ACS Appl, Energy Mater 3 (2020) 9799–9808, https://doi.org/10.1021/acsaem.0c01413.
[33] M.V. de, L. Tinoco, M.B. Costa, L.H. Mascaro, J.F. de Brito, Photoelectrodeposition of Pt nanoparticles on Sb2Se3 photocathodes for enhanced water splitting, Electrochim, Acta 382 (2021), 138290, https://doi.org/10.1016/j.electacta.2021.138290.
[34] Y. Zhou, L. Wang, S. Chen, S. Qin, X. Liu, J. Chen, D.-J. Xue, M. Luo, Y. Cao, Y. Cheng, E.H. Sargent, J. Tang, Thin-film Sb2Se3 photovoltaics with oriented one-dimensional ribbons and benign grain boundaries, Nat. Photonics 9 (2015) 409–415, https://doi.org/10.1038/nphoton.2015.78.
[35] Y. Zhou, M. Leng, Z. Xia, J. Zhong, H. Song, X. Liu, B. Yang, J. Zhang, J. Chen, K. Zhou, J. Han, Y. Cheng, J. Tang, Solution-processed antimony selenide heterojunction solar cells, Adv, Energy Mater 4 (2014), 1301846, https://doi.org/10.1002/aenm.201301846.
[36] C. Chen, W. Li, Y. Zhou, C. Chen, M. Luo, X. Liu, K. Zeng, B. Yang, C. Zhang, J. Han, J. Tang, Optical properties of amorphous and polycrystalline Sb2Se3 thin films prepared by thermal evaporation, Appl, Phys. Lett 107 (2015), 043905, https://doi.org/10.1063/1.4927741.
[37] W.Septina Gunawan, S. Ikeda, T. Harada, M. Higashi, R. Abe, M Matsumura, Photosplitting of water from wide-gap Cu(In,Ga)S2 thin films modified with a CdS layer and Pt nanoparticles for a high-onset-potential photocathode, J. Phys. Chem. C 119 (2015) 8576–8583, https://doi.org/10.1021/acs.jpcc.5b02068.
[38] K. Gelderman, L. Lee, S.W. Donne, Flat-band potential of a semiconductor: using the Mott–Schottky equation, J. Chem. Educ 84 (2007) 685, https://doi.org/10.1021/ed084p685.
[39] O. Madelung, Semiconductors: Data Handbook, 3rd ed., Springer, New York, 2004.
[40] R. Beranek, (Photo)electrochemical methods for the determination of the band edge positions of TiO2-based nanomaterials, Adv, Phys. Chem 2011 (2011) 1–20, https://doi.org/10.1155/2011/786759.
[41] L. Wang, C. Lee, P Schmuki, Solar water splitting: preserving the beneficial small feature size in porous a-Fe2O3 photoelectrodes during annealing, J. Mater. Chem. A 1 (2013) 212–215, https://doi.org/10.1039/c2ta00431c.
[42] A.L. Woodley, C.F. Drury, W.D. Reynolds, W. Calder, X.M. Yang, T.O. Oloya, Improved acid trap methodology for determining ammonia volatilization in wind tunnel experiments, Can, J. Soil Sci 98 (2018) 193–199, https://doi.org/10.1139/cjss-2017-0081.
[43] R.R. Prabhakar, W. Septina, S. Siol, T. Moehl, R. Wick-Joliat, S.D. Tilley, Photocorrosion-resistant Sb2Se3 photocathodes with earth abundant MoS:X hydrogen evolution catalyst, J. Mater. Chem. A 5 (2017) 23139–23145, https://doi.org/10.1039/c7ta08993g.
[44] L. Guo, B. Zhang, S. Li, A. Montgomery, L. Li, G. Xing, Q. Zhang, X. Qian, F. Yan, Interfacial engineering of oxygenated chemical bath e deposited CdS window layer for highly efficient Sb2Se3 thin-film solar cells, Mater, Today Phys 10 (2019), 100125, https://doi.org/10.1016/j.mtphys.2019.100125.
[45] A. Shongalova, D. De Física, U. De Aveiro, On the identification of Sb2Se3 using Raman scattering, MRS Commun 8 (2018) 865–870, https://doi.org/10.1557/mrc.2018.94.
[46] Z. Li, X. Chen, H. Zhu, J. Chen, Chong Zhang, Y. Guo, W. Zhang, X. Niu, Y. Mai, Sb2Se3 thin film solar cells in substrate configuration and the back contact selenization, Sol. Energy Mater. Sol. Cells 161 (2017) 190–196, https://doi.org/10.1016/j.solmat.2016.11.033.
[47] A. Dychalska, P. Popielarski, W. Franków, K. Fabisiak, K. Paprocki, M. Szybowicz, Study of CVD diamond layers with amorphous carbon admixture by Raman scattering spectroscopy, Mater. Sci. 33 (2015) 799–805, https://doi.org/10.1515/msp-2015-0067.
[48] N.B. Singh, U. Sarkar, Structure, vibrational, and optical properties of platinum cluster: a density functional theory approach, J. Mol. Model 20 (2537) (2014) 1–11, https://doi.org/10.1007/s00894-014-2537-5.
[49] N.S. Resende, C.A. Perez, J.G. Eon, M. Schmal, The effect of coating TiO2 on the CO oxidation of the Pt/γ-alumina catalysts, Catal, Letters 141 (2011) 1685–1692, https://doi.org/10.1007/s10562-011-0695-y.
[50] A. Hankin, F.E. Bedoya-Lora, J.C. Alexander, A. Regoutz, G.H. Kelsall, Flat band potential determination: avoiding the pitfalls, J. Mater. Chem. A 7 (2019) 26162–26176, https://doi.org/10.1039/c9ta09569a.
[51] E. Zarei, R. Ojani, Fundamentals and some applications of photoelectrocatalysis and effective factors on its efficiency: a review, J. Solid State Electrochem 21 (2017) 305–336, https://doi.org/10.1007/s10008-016-3385-2.
[52] T.-A. Bu, Y.-C. Hao, W.-Y. Gao, X. Su, L.-W. Chen, N. Zhang, A.-X. Yin, Promoting photocatalytic nitrogen fixation with alkali metal cations and plasmonic nanocrystals, Nanoscale 11 (2019) 10072–10079, https://doi.org/10.1039/C9NR02502B.
[53] J.F. Brito, C. Genovese, F. Tavella, C. Ampelli, M.V.B. Zanoni, G. Centi, S. Perathoner, CO2 reduction of hybrid Cu2O-Cu/Gas Diffusion Layer electrodes and their Integration in a Cu-based photoelectrocatalytic cell, ChemSusChem 12 (2019) 4274–4284, https://doi.org/10.1002/cssc.201901352.
[54] M. Vu, M. Sakar, T. Do, Insights into the recent progress and advanced materials for photocatalytic nitrogen fixation for ammonia (NH3) production, Catalysts 8 (2018) 621–646, https://doi.org/10.3390/catal8120621.
[55] M. Mokhtarimehr, S.A. Tatarkova, Photocurrent transients of thin-film solar cells, J. Opt. Soc. Am. B 34 (2017) 1705–1712, https://doi.org/10.1364/josab.34.001705.
[56] Q. Shen, J. Ma, X. Huang, N. Yang, G. Zhao, Enhanced carbon dioxide conversion to formate on a multi-functional synergistic photoelectrocatalytic interface, Appl, Catal. B Environ 219 (2017) 45–52, https://doi.org/10.1016/j.apcatb.2017.07.029.
[57] S. Xie, Q. Zhang, G. Liu, Y. Wang, Photocatalytic and photoelectrocatalytic reduction of CO2 using heterogeneous catalysts with controlled nanostructures, Chem, Commun 52 (2016) 35–59, https://doi.org/10.1039/C5CC07613G.
[58] D. Zhu, L. Zhang, R.E. Ruther, R.J. Hamers, Photo-illuminated diamond as a solid-state source of solvated electrons in water for nitrogen reduction, Nat. Mater. 12 (2013) 836–841, https://doi.org/10.1038/nmat3696.
[59] J.M. Walls, J.S. Sagu, K.G.U. Wijayantha, Microwave synthesised Pd–TiO2 for photocatalytic ammonia production, RSC Adv. 9 (2019) 6387–6394, https://doi.org/10.1039/c8ra09762c.
[60] M. Thangamuthu, C. Santschi, O.J.F. Martin, Photocatalytic ammonia production enhanced by a plasmonic near-field and hot electrons originating from aluminium nanostructures, Faraday Discuss 214 (2019) 399–415, https://doi.org/10.1039/C8FD00146D.